Available online at www.sciencedirect.com
ScienceDirect
Journal of Computational Physics 227 (2007) 1372–1386
JOURNAL OF COMPUTATIONAL PHYSICS
www.elsevier.com/locate/jcp

ELLAM for resolving the kinematics of two-dimensional resistive magnetohydrodynamic flows

Jiangguo Liu [a,*], Simon Tavener [a], Hongsen Chen [b]

[a] Department of Mathematics, Colorado State University, Fort Collins, CO 80523-1874, USA
[b] Institute for Scientific Computation, Texas A&M University, College Station, TX 77843-3404, USA

Received 18 September 2006; received in revised form 18 April 2007; accepted 6 September 2007
Available online 21 September 2007

Abstract

We combine the finite element method with the Eulerian–Lagrangian Localized Adjoint Method (ELLAM) to solve the convection–diffusion equations that describe the kinematics of magnetohydrodynamic flows, i.e., the advection and diffusion of a magnetic field. Simulations of three two-dimensional test problems are presented and in each case we analyze the energy of the magnetic field as it evolves towards its equilibrium state. Our numerical results highlight the accuracy and efficiency of the ELLAM approach for convection-dominated problems.

PACS: 65M25; 65M60; 76R10; 76R50; 76W05

Keywords: Characteristic method; Convection–diffusion equation; ELLAM; Finite element method; Kinematics; Magnetohydrodynamics (MHD); Resistivity

1. Resistive MHD equations

Magnetohydrodynamics is the study of the interactions between magnetic fields and flows of electrically conducting fluids, typically liquid metals or plasmas. The equations governing MHD are a combination of the Navier–Stokes equations for fluid motion and the Maxwell equations for electromagnetism. The simplest MHD model is that of ideal MHD, which ignores the magnetic diffusion (resistivity). When the diffusion terms are retained, the model is referred to as resistive MHD.

We consider the flow of an inviscid conducting fluid in a magnetic field. Let ρ be the density of the liquid metal or plasma, $\mathbf{v}$ be its velocity, $\mathbf{B}$ the magnetic field, E the total energy density, and ε_m the magnetic diffusion coefficient. We use $|\cdot|$ for the Euclidean 2-norm of a vector and $\otimes$ for the tensor product of two vectors. The equations of conservation of mass, momentum, and energy of the fluid motion are, respectively [10,27],

* Corresponding author. Tel.: +1 970 491 3067; fax: +1 970 491 2161.
E-mail addresses: liu@math.colostate.edu (J. Liu), tavener@math.colostate.edu (S. Tavener), hchen@isc.tamu.edu (H. Chen).

0021-9991/$ - see front matter
doi:10.1016/j.jcp.2007.09.009

$$\rho_t + \nabla \cdot (\rho \mathbf{v}) = 0, \tag{1}$$

$$(\rho \mathbf{v})_t + \nabla \cdot (\rho \mathbf{v} \otimes \mathbf{v} - \mathbf{B} \otimes \mathbf{B}) + \nabla p^* = \mathbf{0}, \tag{2}$$

$$E_t + \nabla \cdot [(E + p^*)\mathbf{v} - (\mathbf{v} \cdot \mathbf{B})\mathbf{B}] = \varepsilon_m |\nabla \times \mathbf{B}|^2, \tag{3}$$

where the energy E is defined as [13,27]

$$E = \frac{p}{\gamma - 1} + \rho \frac{|\mathbf{v}|^2}{2} + \frac{|\mathbf{B}|^2}{2}. \tag{4}$$

Here $\gamma = c_p/c_v$ is the ratio of specific heats. The total pressure p^* consists of a thermal contribution p (also referred to as the gas pressure) and a magnetic contribution, and can be explicitly written as

$$p^* = p + \frac{|\mathbf{B}|^2}{2}. \tag{5}$$

The magnetic field evolves according to the magnetic field induction equation

$$\mathbf{B}_t = \nabla \times (\mathbf{v} \times \mathbf{B}) + \varepsilon_m \Delta \mathbf{B}, \tag{6}$$

and is divergence-free, i.e.,

$$\nabla \cdot \mathbf{B} = 0, \quad \text{for all } t \geqslant 0. \tag{7}$$

The development of efficient numerical methods for solving MHD problems has been the focus of considerable research effort, see [1,2,5,9,13,17,19,21,27] and the references therein. For the ideal MHD model in which the magnetic diffusion $\varepsilon_m = 0$, these equations can be formulated as a first order hyperbolic system and the whole system solved numerically, see [13]. However, for resistive MHD, due to the nonzero diffusion terms in Eqs. (3) and (6), we ought to investigate approaches other than converting the equations to a first order hyperbolic system.

Similar to the divergence-free condition in incompressible hydrodynamics, a major difficulty in solving the MHD equations is to ensure that the magnetic field is divergence-free. A variety of divergence "cleaning" techniques have been developed in numerical methods for MHD equations, see [2,5,9]. Another approach is to express the magnetic field as the curl of a vector potential $\mathbf{A}$, i.e., to define $\mathbf{B} := \nabla \times \mathbf{A} = \mathbf{curl}\mathbf{A}$. This approach is particularly convenient in two dimensions, where $\mathbf{A} = (0, 0, A_3)$ and $\mathbf{B} = (B_1, B_2, 0) = (\partial A_3/\partial y, -\partial A_3/\partial x, 0)$. If the fluid is incompressible ($\nabla \cdot \mathbf{v} = 0$), then Eq. (6) reduces to the scalar convection–diffusion equation

$$(A_3)_t + \nabla \cdot (\mathbf{v} A_3) - \varepsilon_m \Delta A_3 = 0. \tag{8}$$

In this paper, we focus on the magnetic induction Eq. (8) and develop an efficient numerical method for this equation assuming the velocity field is prescribed and incompressible. We thereby study the kinematics of MHD flows and do not consider the influence of the magnetic field on the velocity field. This idealizes the situation in which the ratio of the Lorentz force to inertia is small. This ratio is also quantified as the *interaction parameter* $N = \sigma |\mathbf{B}|^2 l/(\rho |\mathbf{v}|)$, where σ is the electrical conductivity and l is the characteristic length. A similar assumption is made in [16] to investigate the kinematic dynamo regime of MHD. Apart from the fundamental role of kinematics in MHD, one could solve the magnetic induction equation as part of an operator decomposition process in which the magnetic field is computed based on a given velocity field and the velocity field is then modified in response to the new magnetic field, and the entire process iterated until convergence. Accurate and stable numerical methods are clearly needed in both steps of such an operator decomposition process, as well as efficient strategies for monitoring and controlling coupling errors [7].

Convection-dominated convection–diffusion equations like Eq. (8) arise in many other applications including the transport of solutes in groundwater and surface water and the displacement of oil by fluid injection in oil recovery. Numerical simulations for these problems have to resolve spatial structures like contact discontinuities, current sheets, shocks, or steep fronts. This kind of singularities poses serious challenges to numerical methods. Standard finite difference or finite element methods produce either excessive nonphysical oscillations or extra numerical diffusion, which smears these physical features. ELLAM as well as many other numerical methods, have been developed to meet these challenges.

The rest of this paper is organized as follows. In Section 2, we present the ELLAM finite element method. Section 3 reports numerical experiments on applying the numerical method to three common test cases for MHD eddy flows. The paper is concluded with some discussions in Section 4.

2. ELLAM for convection–diffusion problems

Convection-dominated convection–diffusion equations like Eq. (8) exhibit both hyperbolic features due to the convection dominance ($|\mathbf{v}| \gg \varepsilon_{\mathrm{m}}$) and parabolic features due to the nonzero diffusion $\varepsilon_{\mathrm{m}} \neq 0$. The Eulerian–Lagrangian Localized Adjoint Method (ELLAM) [8,20,25] exploits the hyperbolic features of convection–diffusion equations by employing space-time test functions that are based on the local velocity field. By performing temporal discretization along characteristics, ELLAM is able to reduce the temporal truncation error. As an implicit method, ELLAM is unconditionally stable and hence not subject to the severe restrictions imposed by the Courant–Friedrichs–Lewy (CFL) condition. These factors combine to enable ELLAM to generate accurate and stable numerical solutions even when large time steps are used. Moreover, ELLAM provides a general framework for convection–diffusion-reaction equations and implementations based on finite element methods, wavelet methods, and other numerical methods have been developed [8,14,25]. Russell and Celia [20] provided a recent overview of research on ELLAM and its applications.

In this section, we present a finite element method implementation of ELLAM for the linear convection–diffusion equation. Consider

$$\begin{cases} u_t + \nabla \cdot (\mathbf{v}u - \mathbf{D}\nabla u) = f(\mathbf{x},t), \quad \mathbf{x} \in \Omega, \quad t \in (0,T] \\ \text{with appropriate boundary conditions,} \\ u(\mathbf{x},0) = u_0(\mathbf{x}), \quad \mathbf{x} \in \Omega, \end{cases} \tag{9}$$

where $\Omega \subset \mathbb{R}^d$ $(d = 1,2,3)$ is a domain with boundary $\Gamma := \partial\Omega$. Here $u(\mathbf{x},t)$ is an unknown scalar-valued function, $\mathbf{v}(\mathbf{x},\mathrm{t})$ a prescribed velocity field, $\mathbf{D}(\mathbf{x},t)$ a diffusion-dispersion tensor, and $f(\mathbf{x},t)$ a source/sink term.

Let Γ^{I}, Γ^{O}, and Γ^{N} be, respectively, the inflow, outflow, and noflow boundaries identified by

$$\begin{aligned} \Gamma^{\mathrm{I}} &:= \{\mathbf{x} | \mathbf{x} \in \Gamma, \quad \mathbf{v} \cdot \mathbf{n} < 0\}, \\ \Gamma^{\mathrm{O}} &:= \{\mathbf{x} | \mathbf{x} \in \Gamma, \quad \mathbf{v} \cdot \mathbf{n} > 0\}, \\ \Gamma^{\mathrm{N}} &:= \{\mathbf{x} | \mathbf{x} \in \Gamma, \quad \mathbf{v} \cdot \mathbf{n} = 0\} \end{aligned} \tag{10}$$

where $\mathbf{n}$ is the unit outward normal vector on Γ. Dirichlet, Neumann, or Robin (total flux) conditions can be applied within the ELLAM framework on any of these boundary types [25]. We represent these boundary conditions using the notations

$$\begin{aligned} &u(\mathbf{x},t) = g_1^{\mathrm{type}}(\mathbf{x},t), (\mathbf{x},t) \in \Gamma^{\mathrm{type}} \quad \text{(Dirichlet)}, \\ &-\mathbf{D}\nabla u(\mathbf{x},t) \cdot \mathbf{n} = g_2^{\mathrm{type}}(\mathbf{x},t), (\mathbf{x},t) \in \Gamma^{\mathrm{type}} \quad \text{(Neumann)}, \\ &(\mathbf{v}u - \mathbf{D}\nabla u)(\mathbf{x},t) \cdot \mathbf{n} = g_3^{\mathrm{type}}(\mathbf{x},t), (\mathbf{x},t) \in \Gamma^{\mathrm{type}} \quad \text{(Robin)}, \end{aligned} \tag{11}$$

where $\mathrm{type} = \mathrm{I}, \mathrm{O}, \mathrm{N}$ represents an inflow, outflow, or noflow boundary type, respectively. For the magnetic induction equation, we shall consider both Dirichlet and Neumann boundary conditions, which correspond to the perfectly conducting or the perfectly insulating boundary conditions for the magnetic field, respectively.

Let $0 = t_0 < t_1 < \cdots < t_{n-1} < t_n < \cdots < t_N = T$ be a partition of $[0,T]$ with $\Delta t_n := t_n - t_{n-1}$. We multiply Eq. (9) by test functions $w(x,t)$ that vanish outside the space-time strip $\Omega \times (t_{n-1}, t_n]$ and are discontinuous in time at time t_{n-1}. Integration by parts leads to the weak form

$$\begin{aligned} &\int_\Omega u(\mathbf{x},t_n) w(\mathbf{x},t_n)\,\mathrm{d}\mathbf{x} + \int_{t_{n-1}}^{t_n} \int_\Omega (\mathbf{D}\nabla u) \cdot \nabla w\,\mathrm{d}\mathbf{x}\,\mathrm{d}t + \int_{t_{n-1}}^{t_n} \int_{\partial\Omega} (\mathbf{v}u - \mathbf{D}\nabla u) \cdot \mathbf{n} w\,\mathrm{d}S\,\mathrm{d}t \\ &\quad - \int_{t_{n-1}}^{t_n} \int_\Omega u(w_t + \mathbf{v} \cdot \nabla w)\,\mathrm{d}\mathbf{x}\,\mathrm{d}t = \int_\Omega u(\mathbf{x},t_{n-1}) w(\mathbf{x},t_{n-1}^+)\,\mathrm{d}\mathbf{x} + \int_{t_{n-1}}^{t_n} \int_\Omega (fw)(\mathbf{x},t)\,\mathrm{d}\mathbf{x}\,\mathrm{d}t, \end{aligned} \tag{12}$$

where $\mathrm{d}S$ is the differential element on $\partial\Omega$ and $w(\mathbf{x},t_{n-1}^+) := \lim_{t \to t_{n-1}^+} w(\mathbf{x},t)$ arises from the fact that $w(\mathbf{x},t)$ are discontinuous in time at time t_{n-1}.

ELLAM takes advantage of the hyperbolic features of convection–diffusion equations by requiring that test functions satisfy the adjoint equation

$$w_t + \mathbf{v} \cdot \nabla w = 0. \tag{13}$$

This eliminates the last term on the left side of the weak form and implies that test functions are constants along characteristics defined by initial value problems of ordinary differential equations

$$\begin{cases} \frac{\mathrm{d}\mathbf{y}}{\mathrm{d}s} = \mathbf{v}(\mathbf{y}(s;\mathbf{x},t),s), \\ \mathbf{y}(s;\mathbf{x},t)|_{s=t} = \mathbf{x}. \end{cases} \tag{14}$$

Fig. 1 illustrates a one-dimensional ELLAM test function, which is defined in the space-time strip $\Omega \times (t_{n-1}, t_n]$. It is specified as a piecewise polynomial (in the spatial variables) at time t_n and a constant along each characteristic.

Special considerations must be made when characteristics intersect with the domain boundaries. As illustrated in Fig. 2, we first define $\Gamma_n^{\mathrm{I}} := \Gamma^{\mathrm{I}} \times [t_{n-1}, t_n]$, $\Gamma_n^{\mathrm{O}} := \Gamma^{\mathrm{O}} \times [t_{n-1}, t_n]$, and $\Gamma_n^{\mathrm{N}} := \Gamma^{\mathrm{N}} \times [t_{n-1}, t_n]$. For any $\mathbf{x} \in \Omega$, if $(\mathbf{x}, t_n)$ backtracks along a characteristic to $(\mathbf{x}^*, t^*) \in \Gamma_n^{\mathrm{I}}$ (where $t^* > t_{n-1}$), we define $\Delta t^{\mathrm{I}}(\mathbf{x}, t_n) := t_n - t^*$. Otherwise $\Delta t^{\mathrm{I}}(\mathbf{x}, t_n) := t_n - t_{n-1}$. Similarly, if any $(\mathbf{y}, t) \in \Gamma_n^{\mathrm{O}}$ backtracks along a characteristic to $(\mathbf{y}^*, t^*) \in \Gamma_n^{\mathrm{I}}$ (for $t^* > t_{n-1}$), we define $\Delta t^{\mathrm{O}}(\mathbf{y}, t) := t - t^*$. Otherwise $\Delta t^{\mathrm{O}}(\mathbf{y}, t) := t - t_{n-1}$. All four cases are shown in Fig. 2 where

- A_1B_1 goes from the domain to the domain;
- A_2D_1 goes from the domain to the outflow boundary;
- C_1B_2 goes from the inflow boundary to the domain; and
- C_2D_2 goes from the inflow boundary to the outflow boundary.

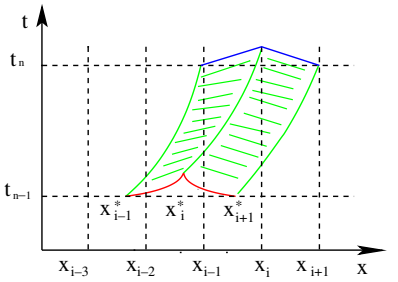

Fig. 1. An illustration of a one-dimensional ELLAM test function, where x_{i-1}^*, x_i^*, x_{i+1}^* are the feet of the characteristics emanating from x_{i-1}, x_i, x_{i+1}.

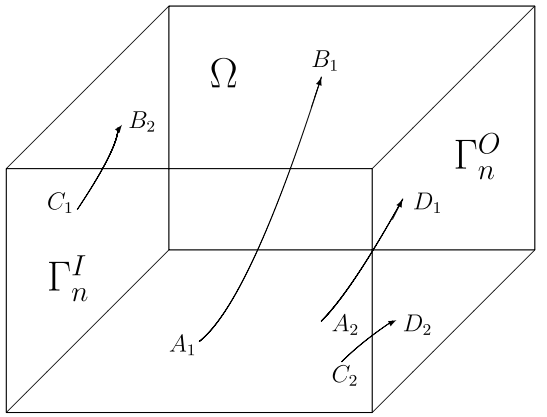

Fig. 2. Characteristics and flows.

By employing the backward Euler quadrature on Ω at time t_n and Γ_n^{O}, the second term on the right side of (12) becomes

$$\int_{t_{n-1}}^{t_n}\int_{\Omega} f(\mathbf{x},t)w(\mathbf{x},t)\,\mathrm{d}\mathbf{x}\,\mathrm{d}t = \int_{\Omega}\Delta t^{\mathrm{I}}(\mathbf{x},t_n)f(\mathbf{x},t_n)w(\mathbf{x},t_n)\,\mathrm{d}\mathbf{x} + \int_{\Gamma_n^{\mathrm{O}}}\Delta t^{\mathrm{O}}(\mathbf{y},t)f(\mathbf{y},t)w(\mathbf{y},t)(\mathbf{v}\cdot\mathbf{n})\,\mathrm{d}S + E(f,w),$$

where $E(f,w)$ is a truncation error term [25]. Similarly, the diffusion term can be evaluated as

$$\begin{aligned}\int_{t_{n-1}}^{t_n}\int_{\Omega}((\mathbf{D}\nabla u)\cdot\nabla w)(\mathbf{x},t)\,\mathrm{d}\mathbf{x}\,\mathrm{d}t &= \int_{\Omega}\Delta t^{\mathrm{I}}(\mathbf{x},t_n)((\mathbf{D}\nabla u)\cdot\nabla w)(\mathbf{x},t_n)\,\mathrm{d}\mathbf{x}\\ &\quad+\int_{\Gamma_n^{\mathrm{O}}}\Delta t^{\mathrm{O}}(\mathbf{y},t)((\mathbf{D}\nabla u)\cdot\nabla w)(\mathbf{y},t)(\mathbf{v}\cdot\mathbf{n})\,\mathrm{d}S + E(\mathbf{D},u,w),\end{aligned}$$

where $E(\mathbf{D},u,w)$ is an error term.

As discussed in [24,25], the error terms $E(f,w)$ and $E(\mathbf{D},u,w)$ are small under certain regularity conditions on the given data. Dropping the error terms in the source and diffusion terms and breaking up the boundary term, we obtain the following problem: Find $u(\mathbf{x},t)\in H^1(\Omega\times(t_{n-1},t_n])$ such that for any $w(\mathbf{x},t)\in H^1(\Omega\times(t_{n-1},t_n])$ satisfying the adjoint Eq. (13),

$$\begin{aligned}&\int_{\Omega}u(\mathbf{x},t_n)w(\mathbf{x},t_n)\,\mathrm{d}\mathbf{x} + \int_{\Omega}\Delta t^{\mathrm{I}}(\mathbf{x},t_n)(\mathbf{D}\nabla u\cdot\nabla w)(\mathbf{x},t_n)\,\mathrm{d}\mathbf{x} + \int_{\Gamma_n^{\mathrm{O}}}\Delta t^{\mathrm{O}}(\mathbf{y},t)(\mathbf{D}\nabla u)\cdot\nabla w)(\mathbf{y},t)(\mathbf{v}\cdot\mathbf{n})\,\mathrm{d}S\\ &\quad+\int_{\Gamma_n^{\mathrm{O}}}(\mathbf{v}u-\mathbf{D}\nabla u)\cdot\mathbf{n}w(\mathbf{y},t)\,\mathrm{d}S + \int_{\Gamma_n^{\mathrm{I}}}(\mathbf{v}u-\mathbf{D}\nabla u)\cdot\mathbf{n}w(\mathbf{y},t)\,\mathrm{d}S\\ &\quad=\int_{\Omega}u(\mathbf{x},t_{n-1})w(\mathbf{x},t_{n-1}^{+})\,\mathrm{d}\mathbf{x} + \int_{\Omega}\Delta t^{\mathrm{I}}(\mathbf{x},t_n)f(\mathbf{x},t_n)w(\mathbf{x},t_n)\,\mathrm{d}\mathbf{x} + \int_{\Gamma_n^{\mathrm{O}}}\Delta t^{\mathrm{O}}(\mathbf{y},t)f(\mathbf{y},t)w(\mathbf{y},t)(\mathbf{v}\cdot\mathbf{n})\,\mathrm{d}S.\end{aligned}\tag{15}$$

For the first term on the right side of (15), replacing the dummy variable $\mathbf{x}$ by $\mathbf{x}^*$, we rewrite the term as

$$\int_{\Omega}u(\mathbf{x}^*,t_{n-1})w(\mathbf{x}^*,t_{n-1}^{+})\,\mathrm{d}\mathbf{x}^* = \int_{\Omega}u(\mathbf{x}^*,t_{n-1})w(\mathbf{x},t_n)\mathbf{J}(\mathbf{x}^*,\mathbf{x})\,\mathrm{d}\mathbf{x},\tag{16}$$

where $\mathbf{x}^*=\mathbf{y}(t_{n-1};\mathbf{x},t_n)$ is obtained by backtracking $(\mathbf{x},t_n)$ along a characteristic to time t_{n-1} and $\mathbf{J}(\mathbf{x}^*,\mathbf{x})$ is the Jacobian.

It is known from the discussion in [15] that for a backtracking characteristic $\mathbf{y}=\mathbf{y}(s;\mathbf{x},t),\ s\leqslant t$,

$$\exp\left(-\int_s^t\|\nabla\cdot\mathbf{v}(\cdot,r)\|_{\infty}\,\mathrm{d}r\right)\leqslant\mathbf{J}(\mathbf{y},\mathbf{x})\leqslant\exp\left(\int_s^t\|\nabla\cdot\mathbf{v}(\cdot,r)\|_{\infty}\,\mathrm{d}r\right),\tag{17}$$

so we have

$$\mathbf{J}(\mathbf{x}^*,\mathbf{x}) = 1+\mathcal{O}(\Delta t).$$

In particular, $\mathbf{J}(\mathbf{x}^*,\mathbf{x})=1$ in (16), if the velocity field is divergence-free. Otherwise, there will be some delicate technical treatments for computing the Jacobian.

As discussed in [4,25], the first term on the right side of the reference Eq. (15) can also be evaluated based on forward tracking along characteristics of finite element quadrature points.

Error estimates about ELLAM can be found in [24] and the references therein. It is proved in [24] that under the following assumptions

(1) $\mathbf{D}=D(\mathbf{x},t)\mathbf{I}_{2\times 2}$ and there exist positive constants $D_{\min}$ and $D_{\max}$ such that $0<D_{\min}\leqslant D(\mathbf{x},t)\leqslant D_{\max}<\infty,\ \forall(\mathbf{x},t)\in\overline{\Omega}\times[0,T]$,
(2) $D(\mathbf{x},t),f(\mathbf{x},t)\in W_{\infty}^1(\Omega\times(0,T))$ and $\mathbf{v}(\mathbf{x},t)\in(W_{\infty}^1(\Omega\times(0,T)))^2$,
(3) The solution $u(\mathbf{x},t)\in L_{\infty}(0,T;W_{\infty}^2(\Omega))$ and $u_t(\mathbf{x},t)\in L_2(0,T;H^2(\Omega))$.

ELLAM with bilinear elements on a rectangular mesh for the two-dimensional convection–diffusion Eq. (9) has the following error estimates

$$\|U_T^{h,\Delta t}(\mathbf{x}) - u_T(\mathbf{x})\|_{L^2(\Omega)} \leqslant C(h^2 + \Delta t),$$

where C is a constant independent of h and Δt.

Summarizing, ELLAM is an efficient method for solving convection-dominated convection–diffusion problems owing to the following features.

(1) Relatively large time steps can be used since ELLAM is not subject to the severe restrictions imposed by the CFL condition.
(2) In situations when convection dominates, the discrete linear system is well-conditioned requiring no preconditioning for iterative solvers.
(3) Interpreting the unknown function as the concentration of a substance being transported by a flow, it has been shown [8,25] that ELLAM is globally mass-conservative.
(4) Since the adjoint equation governing the test functions carries information along characteristics, ELLAM can efficiently resolve steep fronts in solutions without using extremely fine meshes.
(5) As an operator splitting method, ELLAM decouples convection and diffusion processes. Convection is split into the adjoint equation, which becomes an ODE along characteristic directions and is usually solved explicitly. Diffusion is kept in the weak formulation of elliptic type, which is solved implicitly.

For the applications in this paper, we assume Ω is a two-dimensional rectangular domain and $\mathcal{T}_h$ is a rectangular mesh. Let $\mathcal{S}^h = \mathcal{S}^h(\Omega)$ be the finite dimensional subspace of continuous piecewise bilinear polynomials associated with the partition $\mathcal{T}_h$. Approximating $u(\mathbf{x}, t_n)$ from $\mathcal{S}^h$ and taking test functions $w(\mathbf{x}, t_n) \in \mathcal{S}^h$, we obtain a discrete linear system from (15). Furthermore, the coefficient matrix of the linear system is a 9-banded symmetric positive definite matrix and the linear system can be solved by the conjugate gradient method.

3. Numerical experiments

In this section, we report our numerical experiments on three benchmark examples (with slight modifications) that are also studied in [27].

For all three examples, we consider a spatial domain $\Omega = [-0.5, 0.5]^2$ and a time period $[0, T] = [0, 10]$. ELLAM is used with a 64×64 rectangular mesh with bilinear ($\mathcal{Q}_1$) elements and a relatively large time step $\Delta t = 0.1$. The second-order Gaussian quadrature is used in numerical integrations for finite elements. All velocity fields in these three examples are nonlinear, that is, Eq. (14) is a nonlinear ODE in $\mathbf{y}$. Since no explicit expressions are available for finding the characteristics, we employ numerical methods for characteristic tracking. Here we apply the second order Runge–Kutta (Heun method), with 4 micro steps within each macro time step. The three velocity fields we examined are all divergence-free, so $\mathbf{J}(\mathbf{x}^*, \mathbf{x}) = 1$ in Eq. (16), thereby avoiding technical treatments in computing the Jacobian.

The velocity fields for all three examples are shown in Fig. 3. The common initial condition shown in Fig. 4 is

$$(A_3)|_{t=0} = 0.5 - x,$$

which corresponds to an initial (horizontally) uniform magnetic field. The common boundary conditions are posed as

$$(A_3)|_{x=-0.5} = 1, \quad (A_3)|_{x=0.5} = 0, \quad \left.\frac{\partial A_3}{\partial n}\right|_{y=-0.5} = \left.\frac{\partial A_3}{\partial n}\right|_{y=0.5} = 0.$$

Notice that the first two boundary conditions imply that $\mathbf{B} \cdot \mathbf{n} = 0$, i.e., the left and right sides of the rectangular domain are perfectly insulating for the magnetic field. The last two boundary conditions are equivalent to $\mathbf{B} \times \mathbf{n} = \mathbf{0}$, which means the top and bottom sides of the domain are perfectly conducting for the magnetic field.

For each example, we present color images for the magnetic potential function and profiles of the magnetic field lines, i.e., contour plots of the magnetic potential function, at some typical time moments. For the con-

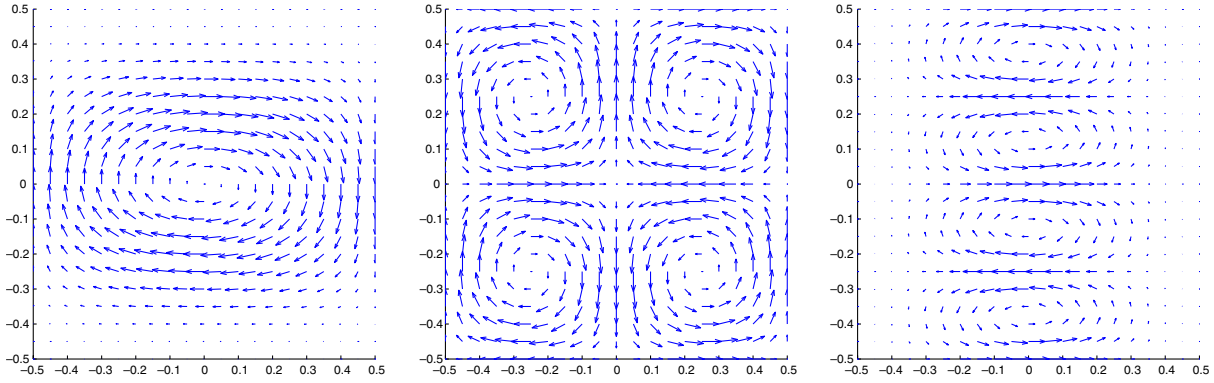

Fig. 3. Quiver plots for the imposed velocity fields in Examples 1–3.

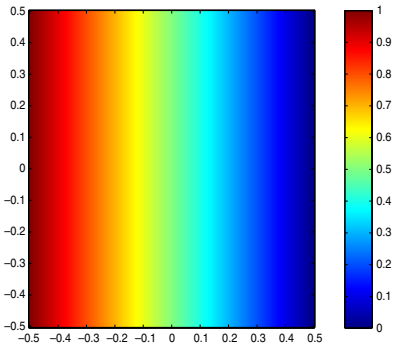

Fig. 4. The common initial condition for all three examples.

tour plots, we use values from 0.0 to 1.0 with an increment 0.05, but only the contours for 0.1, 0.3, 0.5, 0.7, 0.9 are labeled.

Example 1 (*A single eddy*). The velocity field is prescribed as

$$\mathbf{v}(x,y) = \left(\frac{\cos(\pi x)}{\pi} 32y(1-4y^2)^3, -\sin(\pi x)(1-4y^2)^4\right),$$

and is shown in the left subplot of Fig. 3. It has a center at the origin and all four sides of the domain are noflow boundaries. The resistivity $\varepsilon_m = 10^{-3}$.

Given the small value of the resistivity, the magnetic field is strongly convected by the flow and the field lines should be nearly "frozen" in the fluid. Our numerical results clearly show that at the beginning the magnetic field is dragged around by the eddy and the magnetic field energy rises. Then the magnetic flux is expelled away from the single eddy and concentrates around the edges of the eddy, and the field energy decreases. Then the magnetic field approaches its steady state, and the field energy stabilizes for large t, see Fig. 5 and the left subplot of Fig. 9. This phenomenon is known as *flux expulsion* by which the magnetic field in any region of closed streamlines is gradually expelled and is the MHD analogue of the Prandtl–Batchelor theorem for two-dimensional viscous flows.

Example 2 (*A 4-cell convection*). This example dates back to 1966 [10,26,27] as one of the first studies to address the role of the magnetic field in a convecting plasma. Starting from a vertically uniform magnetic field (the initial condition), we simulate the distortion of the magnetic field by a cellular convection. The velocity field is

$$\mathbf{v}(x,y) = (-\sin(2\pi x)\cos(2\pi y), \cos(2\pi x)\sin(2\pi y)),$$

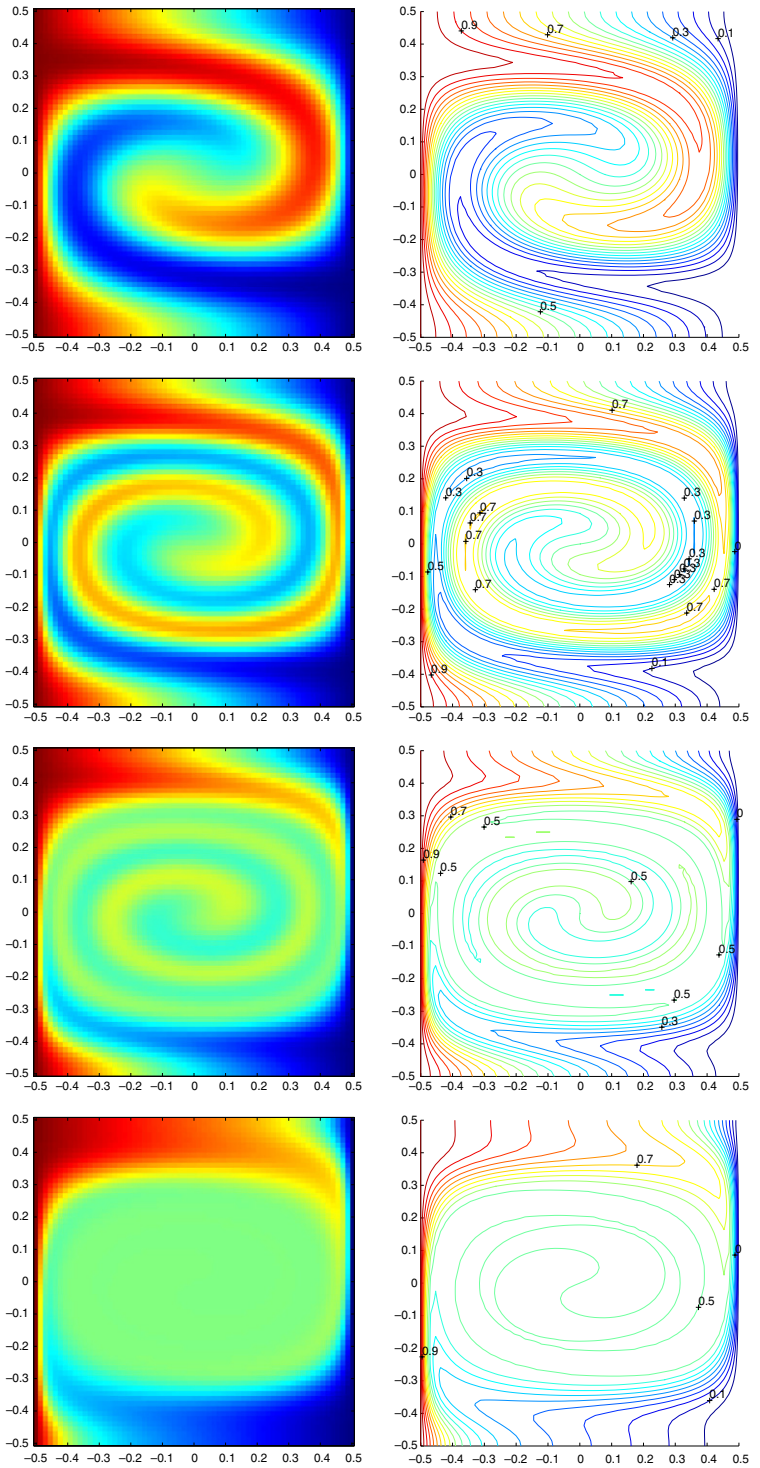

Fig. 5. Plots of the magnetic potential for Example 1 at $t = 1$, 2, 3, and 10.

and is shown in the middle subplot of Fig. 3. It has a saddle point at the origin and four centers located at $(0.25, 0.25)$, $(-0.25, 0.25)$, $(-0.25, -0.25)$, and $(0.25, -0.25)$. All four sides of the domain are again noflow boundaries. The resistivity $\varepsilon_m = 5 \times 10^{-4}$.

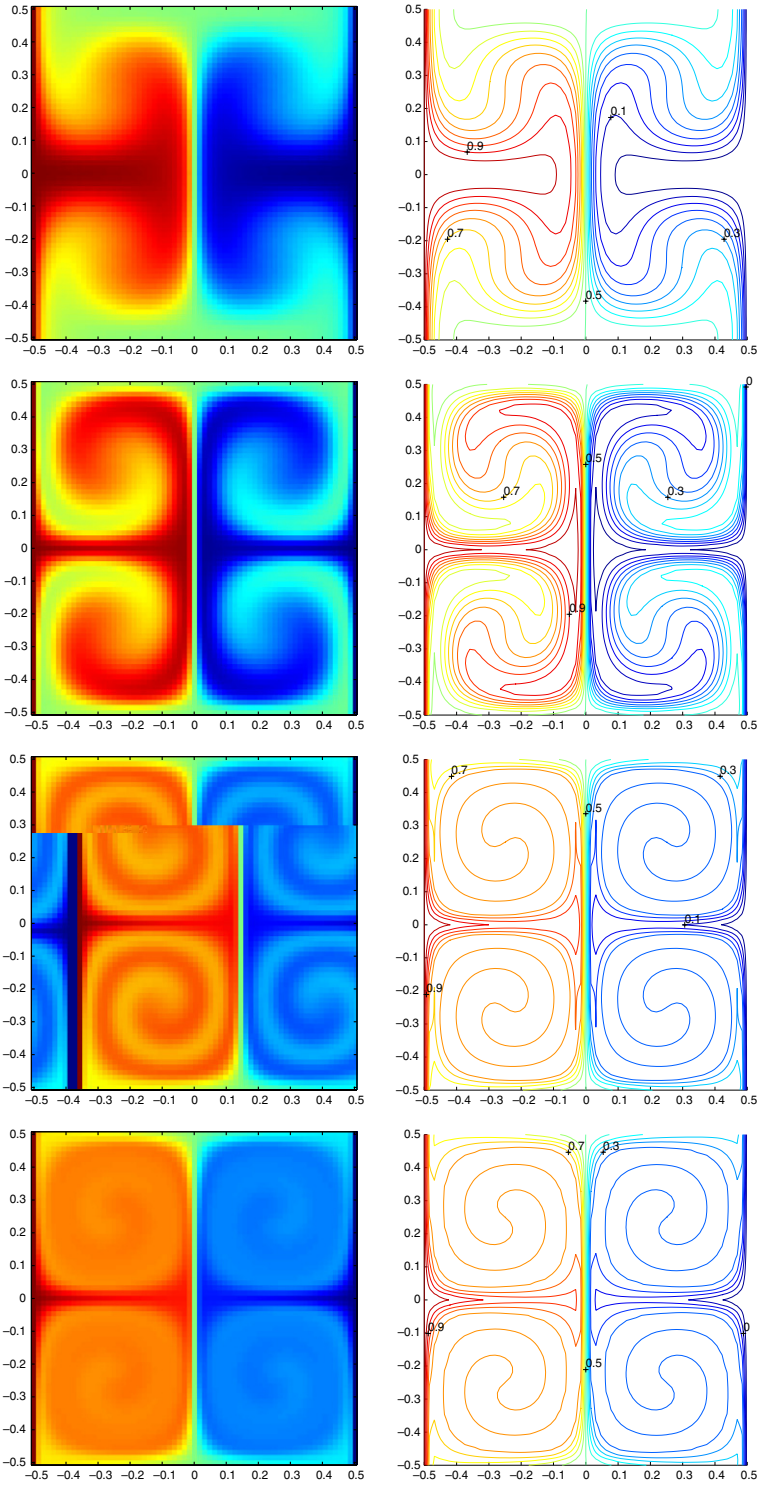

Fig. 6. Plots of the magnetic potential for Example 2 at $t = \frac{1}{2}, 1, 3,$ and 5.

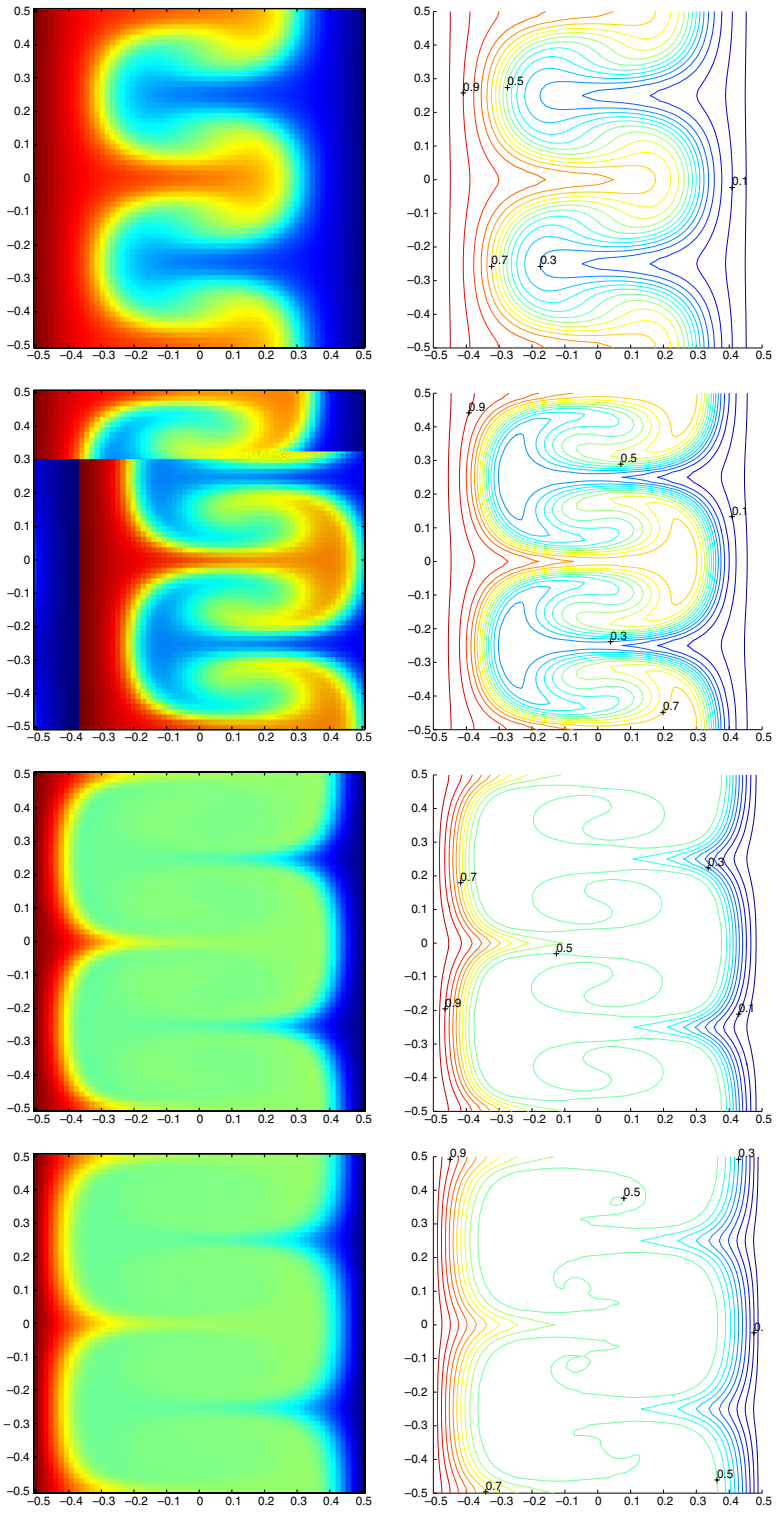

Fig. 7. Plots of the magnetic potential for Example 3 at $t = \frac{1}{2}, 1, 3,$ and 5.

The magnetic field is distorted by the four convective cells. Magnetic reconnection takes place between $t = 1$ and $t = 3$ in the regions of strong currents. The term "magnetic reconnection" refers to a process in which magnetic field lines from different magnetic domains are spliced to one another, changing the overall topology of a magnetic field. In this process, magnetic field energy is converted to plasma kinetic and thermal energy [19].

Example 3 (*A band of* 4 *eddies*). The velocity field is

$$\mathbf{v}(x,y) = \left((1-4x^2)^4\cos(4\pi y), 8x(1-4x^2)^3\frac{\sin(4\pi y)}{\pi}\right),$$

and appears as the right subplot in Fig. 3. The resistivity $\varepsilon_m = 10^{-3}$. Once again we observe the magnetic field lines being convected by the flow, formation of sharp layers, and flux expulsion.

In conclusion, all three examples clearly show the expected formation of boundary and internal layers of width $\mathcal{O}(\sqrt{\varepsilon_m})$ arising due to the dominance of convection over diffusion [18,22]. All three examples show the effect of flux expulsion resulting in magnetic flux becoming concentrated at edges of the convective cells (see Fig. 8).

Recall that the magnetic field energy is defined as

$$\int_\Omega \frac{|\mathbf{B}|^2}{2}\,dx\,dy.$$

With the above discretization, the evolutions of the magnetic field energy in these three examples are shown in Fig. 9. In Example 1, the magnetic field energy reaches its peak at around $t = 1.7$ and then appears to approach a constant or steady-state value as a balance is achieved between convection and diffusion. The two

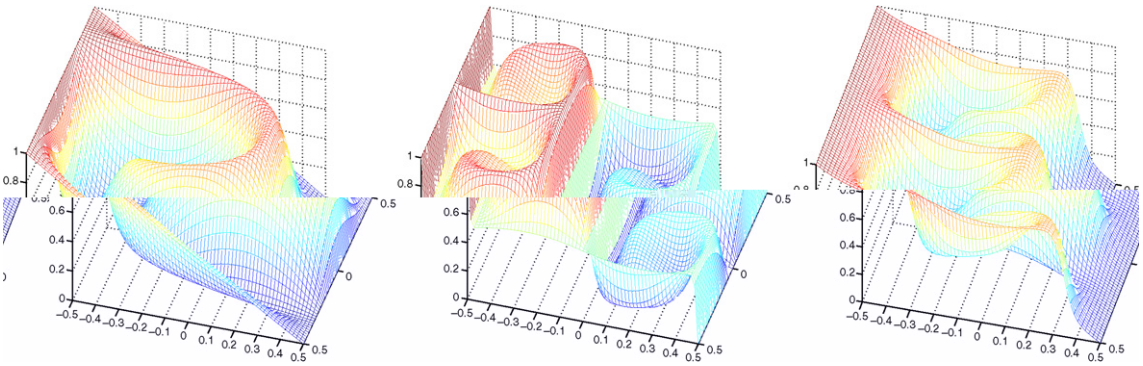

Fig. 8. Sharp fronts exhibited in the solutions of Examples 1–3 at time $t = 1$.

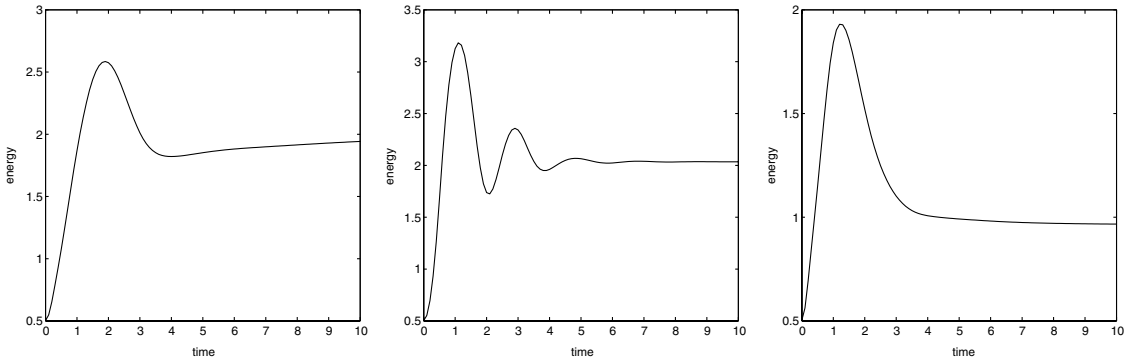

Fig. 9. Time evolution of the magnetic field energy in Examples 1–3.

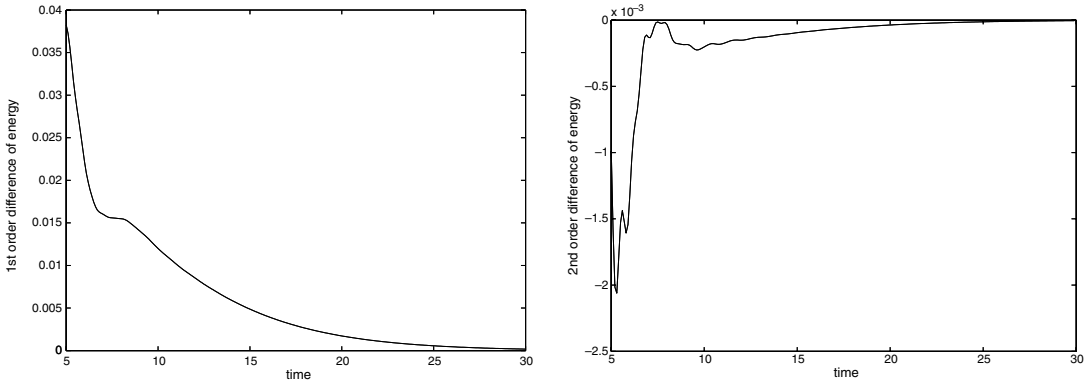

Fig. 10. The first and second order finite differences of the magnetic field energy in Example 1.

plots in Fig. 10 approximate the first and second derivatives of the magnetic field energy for Example 1 for $5 < t < 30$ and confirm the convergence to equilibrium. In Example 2, the field energy shows similar behavior but the oscillations are less well damped. In Example 3, the magnetic field energy reaches its peak at around $t = 1.3$ and then decays towards its equilibrium value. Thus all three examples appear to stabilize and approach their steady-state solutions.

Convergence towards steady-state solutions. In problem (9), if $\mathbf{v}$, $\mathbf{D}$, $\mathbf{f}$ and the boundary conditions do not dependent on t, then the corresponding steady-state convection–diffusion problem is

$$\begin{cases} \nabla \cdot (\mathbf{v}u - \mathbf{D}\nabla u) = f(\mathbf{x}), \quad \mathbf{x} \in \Omega, \\ \text{the same time-independent boundary conditions}, \end{cases} \tag{18}$$

which is *linear* in the unknown scalar u and hence has a unique solution under certain regularity conditions on the given data.

Let $u^T(\mathbf{x})$ be the exact solution of the time-dependent problem (9) at time T and $u^S(\mathbf{x})$ be the exact solution of the steady-state problem (18). Consider the situation in which the time-dependent solution evolves towards the steady-state solution, i.e.,

$$\lim_{T\to\infty} u^T(\mathbf{x}) = u^S(\mathbf{x}), \quad \mathbf{x} \in \Omega. \tag{19}$$

Let $\mathcal{T}_h$ be a quasi-uniform partition of the spatial domain Ω with mesh size h and Δt be the time step size for a partition of the time period $[0, T]$. Furthermore, let $U^T_{h,\Delta t}(\mathbf{x})$ be a numerical solution of the time-dependent problem (9), and $U^S_h(\mathbf{x})$ a numerical solution of the steady-state problem (18). As has been shown in [24], solving the two-dimensional convection–diffusion Eq. (9) using ELLAM with bilinear elements on a rectangular mesh gives rise to the following error estimates

$$\|U^T_{h,\Delta t}(\mathbf{x}) - u^T(\mathbf{x})\|_{L^2(\Omega)} \leqslant C(h^2 + \Delta t), \tag{20}$$

where C is a constant independent of h and Δt. Similar error estimates for the steady-state problem can be found in the literature and hence we have

$$\lim_{h\to 0,\Delta t\to 0} U^T_{h,\Delta t}(\mathbf{x}) = u^T(\mathbf{x}) \quad \text{and} \quad \lim_{h\to 0} U^S_h(\mathbf{x}) = u^S(\mathbf{x}). \tag{21}$$

From (19), (21), and the following inequality

$$\|U^T_{h,\Delta t}(\mathbf{x}) - U^S_h(\mathbf{x})\| \leqslant \|U^T_{h,\Delta t}(\mathbf{x}) - u^T(\mathbf{x})\| + \|u^T(\mathbf{x}) - u^S(\mathbf{x})\| + \|u^S(\mathbf{x}) - U^S_h(\mathbf{x})\|, \tag{22}$$

we expect $\|U^T_{h,\Delta t}(\mathbf{x}) - U^S_h(\mathbf{x})\|$ to be small when T is large enough and $h, \Delta t$ are small enough.

We solve the steady-state problem (18) with the same (time-independent) boundary conditions using bilinear elements on the same rectangular mesh as was used to compute numerical solutions of the time-dependent problem and present comparison results in Table 1. We do not include the plots of the steady-state solutions, since they are graphically indistinguishable from the final time solutions in Figs. 5–7. The convergence of the

Table 1
Comparison of time-dependent numerical solution $U^T_{h,\Delta t}$ and steady-state numerical solution U^S_h: $h = 1/64, \Delta t = 0.1$

$\|U^T_{h,\Delta t} - U^S_h\|$	Example 1		Example 2		Example 3	
	L_∞	L_2	L_∞	L_2	L_∞	L_2
$T = 5$	3.168E−1	6.607E−2	5.322E−2	6.558E−3	4.866E−2	1.167E−2
$T = 10$	1.318E−1	2.707E−2	5.681E−2	6.152E−3	6.668E−3	1.398E−3
$T = 30$	4.393E−2	7.527E−3	5.673E−2	6.161E−3	5.505E−3	1.081E−3

time-dependent solution to the equilibrium solution that is suggested by the plots of the magnetic field energy is supported by the table below.

Notice that the L_∞- and L_2-norms of a continuous piecewise bilinear polynomial on a rectangular mesh can be computed exactly. For each $\mathcal{Q}_1$ element, as a linear combination of the basis functions $1, x, y, xy$, the shape function is a harmonic function and hence satisfies the Maximum Principle. So the L_∞-norm of the piecewise bilinear polynomial is the l_∞-norm of the sequence of its absolute nodal values. The Gram matrix of the basis functions is used to exactly compute the L^2-norm of the shape function. However, the L_1-norm could not be computed exactly, unless the bilinear polynomial does not change sign on the mesh.

4. Discussion

To the best of our knowledge, this study represents the first application of ELLAM to problems arising in magnetohydrodynamics. The three test problems studied here were previously studied in [27] using a moving mesh method. Those computations were performed with an initially uniform rectangular mesh with 70×70 elements and a very small time step size $\Delta t = 10^{-3}$. At each time step, a new mesh is formed by solving a set of elliptic equations in order to minimize a "mesh-energy" functional. The PDEs governing the physics of the flow are then solved by an explicit-implicit numerical method and the resulting discrete linear system solved by BiCGStab. The moving mesh aligns with the features of the solution quite well, but forming the mesh is costly and the mesh calculations also place restrictions on the size of the time step.

In this paper, we apply ELLAM with a similar mesh (64×64 rectangular elements) but with a time step that is two orders of magnitude larger, i.e., $\Delta t = 0.1$, and obtain comparable numerical results. Moreover, no preconditioning is needed for our numerical method due to the fact that the equation is convection-dominated and the linear system after discretization is well-conditioned.

Adaptive treatments can be applied to each of the three major ingredients of the Galerkin finite element framework, namely mesh, trial functions, and test functions. In the static adaptive mesh refinement (*h*-refinement) methods, the locations of a majority of nodes/elements are fixed. Few nodes are added or removed based on some *a posteriori* error estimates. The moving mesh techniques (*r*-refinement) investigated in [3,12,27] (and the references therein) dynamically form a new mesh for each time step based on a mesh-energy functional. The *p*-refinement techniques adaptively adjust the degree of the polynomials in trial functions. ELLAM relies on "smart" test functions that carry adaptivity information along the directions of streamlines. The efficiency of ELLAM could be further enhanced by incorporating *h*-refinement techniques. This is being investigated and will be reported in our future work.

Spectral methods usually perform very well when solving differential equations with homogeneous or periodic boundary conditions on tensor-product type meshes. As discussed in [6,23], the global nature of the spectral methods has delayed their development for problems exhibiting very localized phenomena, such as sharp fronts and boundary layers in convection-dominated diffusion equations, or shock waves in hyperbolic problems. In these situations, the spectral accuracy must be balanced against severe stability requirements. A spectral method combined with characteristic tracking for hyperbolic problems and convection–diffusion problems was developed in [23] under the restrictions of periodic boundary conditions and rectangular meshes. Spectral methods for hyperbolic problems and convection–diffusion problems on unstructured grids were presented in [11]. The convective operator results in a restriction on the time-step that is necessary to maintain stability of the spectral methods. ELLAM discussed in this paper is an efficient numerical method specially designed for convection-dominated diffusion problems. It naturally incorporates unstructured meshes and all kinds of

boundary conditions in its formulation, has the optimal approximation accuracy (not the spectral accuracy though), and is unconditionally stable.

As shown in this paper, the divergence-free property of the magnetic field is an important physical property that should be respected by numerical methods. Besides introducing a scalar/vector potential, another approach is to use the locally divergence-free (LDF) finite elements. Then the discontinuous Galerkin method comes into play very naturally. Combining the LDF finite elements and the discontinuous Galerkin method to solve the ideal MHD equations has been reported in [13]. We are investigating solution techniques for the resistive MHD based on the discontinuous Galerkin method and the LDF finite elements.

The three test cases presented in this paper demonstrate the one-way coupling of the velocity $\mathbf{v}$ on the magnetic field $\mathbf{B}$. In our future work, we will further investigate computations of the velocity field given the magnetic field, and convergence and error control of iterative schemes to solve the fully coupled nonlinear MHD problems.

Acknowledgment

The authors would like to express their sincere thanks to the referees for their very valuable comments and suggestions, which greatly improved the quality of this paper.

References

[1] A. Alexakis, P.D. Mininni, A.G. Pouquet, Shell-to-shell energy transfer in magnetohydrodynamics. I. Steady state turbulence, Phys. Rev. E 72 (3) (2005), no. 4, 046301, 10 pp.
[2] D.S. Balsara, D.S. Spicer, A staggered mesh algorithm using high order Godunov fluxes to ensure solenoidal magnetic fields in magnetohydrodynamic simulations, J. Comput. Phys. 149 (1999) 270–292.
[3] G. Beckett, J.A. Mackenzie, A. Ramage, D.M. Sloan, Computational solution of two-dimensional unsteady PDEs using moving mesh methods, J. Comput. Phys. 182 (2002) 478–495.
[4] P. Binning, M.A. Celia, A forward particle tracking Eulerian–Lagrangian localized adjoint method for solution of the contaminant transport equation in three dimensions, Adv. Water Res. 25 (2002) 147–157.
[5] J.U. Brackbill, D.C. Barnes, The effect of nonzero $\nabla \cdot B$ on the numerical solution of the magnetohydrodynamic equations, J. Comput. Phys. 35 (1980) 426–430.
[6] C. Canuto, M.Y. Hussaini, A. Quarteroni, T.A. Zang, Spectral Methods in Fluid Mechanics, Springer-Verlag, 1987.
[7] V. Carey, D. Estep, S. Tavener, A posteriori analysis and adaptive error control for operator decomposition of elliptic systems I: triangular systems. SIAM J. Numer. Anal. (submitted for publication).
[8] M.A. Celia, T.F. Russell, I. Herrera, R.E. Ewing, An Eulerian–Lagrangian localized adjoint method for the advection–diffusion equation, Adv. Water Res. 13 (1990) 187–206.
[9] W. Dai, P.R. Woodward, A simple finite difference scheme for multidimensional magnetohydrodynamical equations, J. Comput. Phys. 142 (1998) 331–369.
[10] P.A. Davidson, An Introduction to Magnetohydrodynamics, Cambridge University Press, 2001.
[11] J.S. Hesthaven, C.H. Teng, Stable spectral methods on tetrahedral elements, SIAM J. Sci. Comput. 21 (2000) 2352–2380.
[12] W. Huang, R.D. Russell, Moving mesh strategy based on a gradient flow equation for two-dimensional problems, SIAM J. Sci. Comput. 20 (1999) 998–1015.
[13] F. Li, C.W. Shu, Locally divergence-free discontinuous Galerkin methods for MHD equations, J. Sci. Comput. 22/23 (2005) 413–442.
[14] J. Liu, R.E. Ewing, G. Qin, Multilevel numerical solutions of convection-dominated diffusion problems by spline wavelets, Numer. Meth. PDEs 22 (2006) 994–1006.
[15] J. Liu, B. Popov, H. Wang, R.E. Ewing, Convergence analysis of wavelet schemes for convection-reaction equations under minimal regularity assumptions, SIAM J. Numer. Anal. 43 (2005) 521–539.
[16] P.D. Mininni, A. Alexakis, A.G. Pouquet, Shell-to-shell energy transfer in magnetohydrodynamics. II. Kinematic dynamo, Phys. Rev. E 72 (3) (2005), no. 4, 046302, 8 pp.
[17] P.D. Mininni, D.C. Montgomery, A.G. Pouquet, A numerical study of the alpha model for two-dimensional magnetohydrodynamic turbulent flows, Phys. Fluids 17 (2005), no. 3, 035112, 17 pp.
[18] K.W. Morton, Numerical Solution of Convection–diffusion Problems, Chapman and Hall, 1996.
[19] D.R. Reynolds, R. Samtaney, C.S. Woodward, A fully implicit numerical method for single-fluid resistive magnetohydrodynamics, J. Comput. Phys. 219 (2006) 144–162.
[20] T.F. Russell, M.A. Celia, An overview of research on Eulerian–Lagrangian localized adjoint methods (ELLAM), Adv. Water Res. 25 (2002) 1215–1231.
[21] T.W.H. Sheu, R.K. Lin, Development of a convection–diffusion-reaction magnetohydrodynamic solver on non-staggered grids, Inter. J. Numer. Meth. Fluids 45 (2004) 1209–1233.
[22] M. Stynes, Steady-state convection–diffusion problems, Acta Numer. 14 (2005) 445–508.

[23] E. Süli, A. Ware, A spectral method of characteristics for hyperbolic problems, SIAM J. Numer. Anal. 28 (1991) 423–445.
[24] H. Wang, An optimal-order error estimate for an ELLAM scheme for two-dimensional linear advection–diffusion equations, SIAM J. Numer. Anal. 37 (2000) 1338–1368.
[25] H. Wang, H.K. Dahle, R.E. Ewing, M.S. Espedal, R.C. Sharpley, S. Man, An ELLAM scheme for advection–diffusion equations in two dimensions, SIAM J. Sci. Comput. 20 (1999) 2160–2194.
[26] N.O. Weiss, The expulsion of magnetic flux by eddies, Proc. Roy. Soc. A 293 (1966) 310–328.
[27] P.A. Zegeling, On resistive MHD models with adaptive moving meshes, J. Sci. Comput. 24 (2005) 263–284.